

IMAGE VARIFOLDS ON MESHES FOR MAPPING SPATIAL TRANSCRIPTOMICS

MICHAEL I. MILLER, ALAIN TROUVÉ, AND LAURENT YOUNES

ABSTRACT. Advances in the development of largely automated microscopy methods such as MERFISH for imaging cellular structures in mouse brains are providing spatial detection of micron resolution gene expression. While there has been tremendous progress made in the field Computational Anatomy (CA) to perform diffeomorphic mapping technologies at the tissue scales for advanced neuroinformatic studies in common coordinates, integration of molecular- and cellular-scale populations through statistical averaging via common coordinates remains yet unattained. This paper describes the first set of algorithms for calculating geodesics in the space of diffeomorphisms, what we term Image-Varifold LDDMM, extending the family of large deformation diffeomorphic metric mapping (LDDMM) algorithms to accommodate the “copy and paste” varifold action of particles which extends consistently to the tissue scales.

We represent the brain data as geometric measures, termed as *image varifolds* supported by a large number of unstructured points, each point representing a small volume in space and carrying a list of densities of *features* elements of a high-dimensional feature space. The shape of image varifold brain spaces is measured by transforming them by diffeomorphisms. The metric between image varifolds is obtained after embedding these objects in a linear space equipped with the norm, yielding a so-called “chordal metric.”

1. INTRODUCTION

We are seeing a new period of method-driven renaissance in neuroanatomy, one that is distinguished by a focus on large-scale projects generating unprecedented amounts of spatially resolved brain data across multiple, complementary modalities. Recent years have seen many advances in the development of largely automated microscopy instruments for imaging cellular structures in mouse brain anatomy and function [34, 36, 38, 54], including morphological reconstructions at the dense 3D electron microscopy (EM) [18] and at the mesoscale by whole-brain reconstructions (as exemplified by the BRAIN Cell Census Network (BICCN) project [14]), neuronal projectomes [35, 55] and brain-wide maps of cell type distributions [24], spatial transcriptomics technologies, such as MERFISH [9, 31, 48], STARmap [22, 47] generating massive amounts of gene expression data of thousands of genes at a time, as well as emergent barcoding technologies linking data on neuronal projectomes with dense transcriptional profiling at the single-cell level [10, 42, 21].

Since the publication of the Allen ISH atlas in 2006, methods for the spatial detection of gene expression have rapidly improved in their both spatial resolution and the number of genes that can be detected simultaneously. A host of different methods, including MERFISH, STARmap, seqFISH [40], and others now allows for the simultaneous measurement of a few hundreds to thousands of genes, and

potentially all genes, at single molecule and hence single-cell resolution, and at the scale of whole brain sections. Spatially resolved transcriptomic data further offers an opportunity for obtaining multi-modal measurements at single-cell resolution allowing for the combination of dense spatial transcriptomics with the simultaneous measurement of single-neuron projection information using barcode sequencing in BARseq2 [10, 42]. Spatial transcriptomics data can also be registered to functional Ca2+ imaging data, linking gene expression and neuronal activity in behaving mice [7, 50, 12]. The importance of these technological advancements for understanding the dense metric structure of the brain by building up coarse physiological atlas scales built up from dense imaging measurements at the cellular scales was recently recognized when spatial transcriptomics was selected as Nature method of the year [49].

While disparate datasets are being collected from comparable brains and thus exist in a common underlying coordinate system, differences in data modalities and imaging technologies however map them into disparate spaces that need to be mapped to each other to allow integration and maximal impact of these datasets obtained under high expense. This is one of the principal goals of this paper to provide image varifold (IV) LDMMM building on the progress made in the Computational Anatomy (CA) [17, 3, 37] community in the suite of methods called large deformation diffeomorphic metric mapping (LDDMM). Advances in CA for diffeomorphic mapping technologies to atlas coordinates at the tissue scales [5, 4, 54, 41] provide mapping technologies for advanced neuroinformatic studies in common coordinates. Integration of molecular scale populations through statistical averaging via common coordinates remains yet unattained at the molecular and cellular scales. Only recently have theories been put forward that extend the diffeomorphism atlasing technologies of CA [29, 30, 17, 3, 37, 5, 4, 54, 41] to the molecular scales consistently with diffeomorphic mapping at the tissue scales, providing mapping technologies for advanced neuroinformatic studies in common coordinates, integration of molecular- and cellular-scale populations through statistical averaging via common coordinates. These theories, introduced in Miller et al. [30, 26], describe the geodesic equations for building correspondences between MERFISH samples using varifold norms. This paper describes the new family of algorithms for calculating these geodesics, what we term Image-Varifold LDDMM, extending the family of large deformation diffeomorphic metric mapping (LDDMM) algorithms [5, 27, 43, 45, 28] to accommodate the copy-and-paste varifold action of particles described in [30] which extends consistently to the tissue scales.

We expect that the Image-Varifold LDDMM technologies will also be important for problems emerging now in digital pathology linking the molecular scales of histology with the tissue scales of MRI for understanding neurodegenerative diseases associated to the validation and further development of biomarkers as surrogates of molecular disease, as in Alzheimer’s Disease [41].

The major contribution of this paper is to adapt advanced computational methods developed in the field of Computational Anatomy for neuroanatomical data analysis by a broad neuroscience research community using spatial transcriptomics datasets. We believe IV-LDDMM can potentially be broadly used by the neuroscience community since we will describe algorithms for registering datasets collected from multiple animals as 3D stacks or as single 2D sections as well as build correspondence to the Common Coordinate Framework (CCF) template [52] that

enables standardized comparisons across different datasets and users. Further, the user will be able to overlay and segment the registered data with labels from atlases transporting the labels from the coarse tissue scale to the fine molecular scale using the diffeomorphic properties of the maps, including the Allen ARA 2008 atlas [23], CCFv3 2017 atlas [13] and the recently built unified Paxinos and CCFv3 atlas [46]. This will allow users will to be able to perform statistical analysis on multiple sections within and across animals to extract a number of useful statistics of their data leveraging the anatomical labels and and the user will be able to share datasets within registered coordinate systems with other groups collaborating on data analysis with different laboratories.

2. IMAGE VARIFOLDS

2.1. Definitions. Let \mathcal{F} denote a “feature” space, which correspond to typically high-dimensional measurements made by the imaging system, describing biological function. We are interested in the combined analysis of space and function, and will therefore work with the product space $\mathbb{R}^d \times \mathcal{F}$ ($d = 2$ or 3).

At macroscopic scale, an image is usually defined, using a continuum approximation, as a function $q : \mathbb{R}^d \rightarrow \mathcal{F}$. However, in biological imaging, the image values, discretized over pixels, result from the accumulated contributions (counts) of various chemical components collected in the imaged volume and are discrete in nature. Mathematically, “counting” is represented using Dirac measures. The elementary Dirac measure $\delta_x \otimes \delta_f$ (for $x \in \mathbb{R}^d$ and $f \in \mathcal{F}$), when evaluated at a set $V \times A$ in $\mathbb{R}^d \times \mathcal{F}$, returns 1 if $x \in V$ and $f \in A$ and zero otherwise. It can be interpreted as an indication that a “basic element” (for example, a protein, or a cell) is observed at location x with feature f (which can be, for example, a protein species or a cell type). The Diracs can be added, taking

$$\mu = \sum_{k=1}^n \delta_{x_k} \otimes \delta_{f_k},$$

so that $\mu(V \times A)$ counts the number of pairs (x_k, f_k) in the $V \times A$ and can be viewed as a microscopic description of the data.

If V is a small volume, the quantity

$$\rho(V) = \frac{1}{|V|} \sum_{k=1}^n \delta_{x_k}(V)$$

where $|V|$ is the volume of V , measures the density of these elements. The quantity

$$\zeta_V = \frac{\sum_{k:x_k \in V} \delta_{f_k}}{\sum_{k=1}^n \delta_{x_k}(V)}$$

then provides a probability measure on \mathcal{F} that describes the feature profile of V . The continuum approximation corresponding to macroscopic scales is obtained by fixing $x \in \mathbb{R}^d$ and letting V_x be an infinitesimal neighborhood of x with volume dx and approximating ζ_{V_x} with ζ_x :

$$(1) \quad \mu(V_x \times A) \simeq \zeta_x(A) \rho(x) dx, \quad A \subset \mathcal{F}.$$

We introduce the following notation. If \mathbf{m} is a measure on \mathbb{R}^d and ζ a transition probability from \mathbb{R}^d to \mathcal{F} (i.e., a function $x \mapsto \zeta_x$ where ζ_x is a probability measure

on \mathcal{F}), we define $\mathbf{m} \bar{\otimes} \zeta$ as the measure such that

$$(2) \quad (\mathbf{m} \bar{\otimes} \zeta)(U \times A) = \int_U \int_A d\zeta_x(f) d\mathbf{m}(x)$$

for all measurable $U \subset \mathbb{R}^d$ and $A \subset \mathcal{F}$. The measure μ in Eq. (1) is equal to $(\rho\boldsymbol{\lambda}) \bar{\otimes} \zeta$, where $\boldsymbol{\lambda}$ denotes Lebesgue's measure, with $d\boldsymbol{\lambda}(x) = dx$. We will refer to measures on $\mathbb{R}^d \times \mathcal{F}$ as *image varifolds*, and this concept provides a unified representation of microscopic and macroscopic scales. Defining “space-feature functions” as mappings $F : \mathbb{R}^d \times \mathcal{F} \rightarrow \mathbb{R}$, image varifolds are linear operators on the set of such functions, with notation

$$(\mu | F) = \int_{\mathbb{R}^d \times \mathcal{F}} F(x, f) d\mu(x, f).$$

We emphasize that any function $q : \mathbb{R}^d \rightarrow \mathcal{F}$ can be considered as an image varifold μ_q such that $q \mapsto \mu_q$ provides a one-to-one representation of measurable functions and for any F , one has

$$(3) \quad (\mu_q | F) = \int_{\mathbb{R}^d} F(x, q(x)) dx.$$

We use diffeomorphisms to transform image varifolds and to define geodesics in the space of image varifolds. Diffeomorphisms act on functions $q : \mathbb{R}^d \rightarrow \mathcal{F}$ as $\varphi \cdot q = q \circ \varphi^{-1}$ with (3) implying

$$\begin{aligned} (\mu_{\varphi \cdot q} | F) &= \int_{\mathbb{R}^d} F(x, q \circ \varphi^{-1}(x)) dx \\ &= \int_{\mathbb{R}^d} |D\varphi| F(\varphi(x), q(x)) dx \\ &= (\mu_q | |D\varphi| F(\varphi(\cdot), \cdot)) \end{aligned}$$

where $|D\varphi|$ is the absolute value of the Jacobian determinant of φ . This suggests defining the action of a diffeomorphism φ on an image varifold as an extension of $\mu_q \rightarrow \mu_{\varphi \cdot q}$, simply letting, for a general varifold μ :

$$(4) \quad (\varphi \cdot \mu | F(\cdot, \cdot)) = (\mu | |D\varphi| F(\varphi(\cdot), \cdot)).$$

The following definition summarizes this discussion.

Definition 1. *Let \mathcal{F} be equipped with a σ -algebra making it a measurable space. A d -dimensional image varifold is a measure on the set $\mathbb{R}^d \times \mathcal{F}$.*

If \mathbf{m} is a measure on \mathbb{R}^d and ζ a transition probability from \mathbb{R}^d to \mathcal{F} , the measure $\mathbf{m} \bar{\otimes} \zeta$ in Eq. (2) is called an image varifold in disintegrated form.

Diffeomorphisms of \mathbb{R}^d act on image varifolds through the action defined in Eq. (4).

Remark 1. In the decomposition of Eq. (2), ζ_x only needs to be defined for x in the support of \mathbf{m} . If ζ is a fixed measure on \mathcal{F} , $\mathbf{m} \bar{\otimes} \zeta$ is the product measure between \mathbf{m} and ζ , in which case we will prefer the standard notation $\mathbf{m} \otimes \zeta$.

The previous discussion provides examples of image varifolds in disintegrated form. First the “continuum image varifolds” takes the form:

$$(5a) \quad \mu = (\rho\boldsymbol{\lambda}) \bar{\otimes} \zeta$$

and the image varifold μ_q for function $q : \mathbb{R}^d \rightarrow \mathcal{F}$ has \mathbf{m} Lebesgue's measure and $\zeta_x = \delta_{q(x)}$. The discrete image varifold

$$(5b) \quad \mu = \sum_{k=1}^n \delta_{x_k} \otimes \delta_{f_k}, \quad x_k \in \mathbb{R}^d, f_k \in \mathcal{F}$$

has $\mathbf{m} = \sum_{k=1}^n \delta_{x_k}$ and $\zeta_x = \delta_{q(x)}$ where $q : \mathbb{R}^d \rightarrow \mathcal{F}$ is any function such that $q(x_k) = f_k$ for $k = 1, \dots, n$. Indeed, we can write, for any functions $F : \mathbb{R}^d \rightarrow \mathbb{R}$ and $G : \mathcal{F} \rightarrow \mathbb{R}$,

$$\begin{aligned} (\mathbf{m} \bar{\otimes} \zeta \mid FG) &= \int_{\mathbb{R}^d} \int_{\mathcal{F}} F(x)G(f)d\zeta_x(f)d\mathbf{m}(x) \\ &= \int_{\mathbb{R}^d} F(x)G(q(x))d\mathbf{m}(x) \\ &= \sum_{k=1}^n F(x_k)G(f_k). \end{aligned}$$

Image varifolds are the main focus of this paper, with a primary goal to develop a numerical approach allowing for their comparison. They have been introduced in [30] as a tool for the analysis of spatially resolved transcriptomic images, in combination with a hierarchical modeling. (We will however only consider a single scale in the present paper.) Varifolds [1] were introduced as a mathematical representation of surfaces (or more generally of Riemannian manifolds), as measures in on the product space $\mathbb{R}^3 \times S^2$, where S^2 (replaced by a Grassmannian for general manifolds) is the unit sphere in \mathbb{R}^3 , in order to facilitate the analysis of variational problems over surfaces. In that original model, the equivalent of \mathbf{m} in Definition 1 is the singular measure supported by a surface $M \subset \mathbb{R}^3$ and ζ_x is, for $x \in M$, the Dirac measure at the normal to M at x . Surface varifolds have been introduced in [8] for shape analysis, and used in conjunction with the LDDMM algorithm to develop surface matching methods.

Remark 2. We point out that an alternate action of diffeomorphisms on varifolds can be defined in which the Jacobian determinant is dropped from the right-hand side of Eq. (4). The resulting action (denoted $\varphi_{\#}\mu$) is the push-forward of the measure μ by φ . The resulting action on images (here interpreted as densities) is $\varphi_{\#}q = |D\varphi^{-1}|q \circ \varphi^{-1}$. This latter action is the one used in shape analysis to compare curves or surfaces [8]. In our setting, where we need to compare tissues with similar compositions but different sizes, this push-forward action is not appropriate, since, say, expansion results in $|D\varphi^{-1}| < 1$ and a reduction of the original density (i.e., a sparsification of cells in tissue), which is undesirable. The action we choose throughout for image varifolds leaves the magnitude of q unchanged, essentially creating more volume without changing the composition of the tissue using a “copy and paste” operation.

2.2. A semi-discrete representation of varifolds. Equation (5b) describes a varifold in full discrete form, which is well adapted for numerical computations. In the following, however, it will be convenient to have more flexibility on the image transition probabilities, allowing them to be non discrete. We still discretize the spatial domain using Dirac measures, but, in preparation for our mesh model in the next section, we attach these measures to small subsets of \mathbb{R}^d and provide them with

weights that depend on the volume of these subsets. This results in “semi-discrete varifolds,” used throughout, defined by

- (i) A finite family, Γ , of subsets of \mathbb{R}^d with a list of “centers,” $m_\gamma \in \gamma$, $\gamma \in \Gamma$, with volumes $|\gamma|$;
- (ii) A list of weights, $\alpha_\gamma \geq 0$, $\gamma \in \Gamma$;
- (iii) A list of probability measures on \mathcal{F} , ζ_γ , $\gamma \in \Gamma$;

Our space of image-varifold $(\Gamma, m, \alpha, \zeta)$ with action via diffeomorphisms becomes

$$(6a) \quad \mu = \sum_{\gamma \in \Gamma} \alpha_\gamma |\gamma| \delta_{m_\gamma} \otimes \zeta_\gamma.$$

$$(6b) \quad \varphi \cdot \mu = \sum_{\gamma \in \Gamma} \alpha_\gamma |D\varphi(m_\gamma)| |\gamma| \delta_{\varphi(m_\gamma)} \otimes \zeta_\gamma.$$

We call these varifolds “semi-discrete” since we use Dirac measures for the spatial component but not necessarily for the image. For a space-feature functions they act linearly on functions on $\mathbb{R}^d \times \mathcal{F}$:

$$(\mu | F) = \sum_{\gamma \in \Gamma} \alpha_\gamma |\gamma| \int_{\mathcal{F}} F(m_\gamma, f) d\zeta_\gamma(f).$$

2.3. Mesh-based varifolds used for computation. We now specialize further to the situation in which the sets in Γ are associated with meshes in \mathbb{R}^d , using simplicial meshes (i.e., tetrahedra in 3D and triangles in 2D). Letting d denote the dimension, (two or three), we define a simplicial family as a collection $\mathbf{x} = (x_i, i \in I)$ of distinct points in \mathbb{R}^d together with a family of $(d + 1)$ -tuples, $C = (c = (c_0, \dots, c_d) \in I^{d+1})$ of indexes such that the simplices

$$\gamma_c(\mathbf{x}) = \left\{ \sum_{i=0}^d a_i x_{c_i}, a_i \geq 0, a_0 + \dots + a_d = 1 \right\}$$

have non-empty interior with positive orientation, i.e., their volume is

$$(7) \quad |\gamma_c(\mathbf{x})| := \det(x_{c_1} - x_{c_0}, \dots, x_{c_d} - x_{c_0}) / d!,$$

requiring that the term in the right-hand side is positive. The simplex centers m_c are

$$m_c(\mathbf{x}) = \frac{1}{d+1} (x_{c_0} + \dots + x_{c_d}).$$

This family forms a simplicial mesh of some subset D of \mathbb{R}^d if the simplices only intersect at faces, edges or vertexes and their union is equal to D , but we will not need to enforce this constraint in this paper. We let $S = (I, C)$, the collection of indexes and $(d + 1)$ -tuples, which represents the structure of the family. We denote the family itself (with a valid instantiation of vertexes) as $(I, C, \mathbf{x}) = (S, \mathbf{x})$.

Let \mathcal{F} denote a feature space, as above.

Definition 2. *A simplicial image varifold structure is given by a simplicial family (S, \mathbf{x}) with $S = (I, C)$, a family non-negative numbers $(\alpha_c, c \in C)$ and a family of probability measures on \mathcal{F} , $\zeta = (\zeta_c, c \in C)$, with everything summarized as $\mathcal{T} = (S, \mathbf{x}, \alpha, \zeta)$. The associated image varifold and the result of its transformation*

by a diffeomorphism φ are

$$(8a) \quad \mu_{\mathcal{T}} = \sum_{c \in \mathcal{C}} \alpha_c |\gamma_c(\mathbf{x})| \delta_{m_c(\mathbf{x})} \otimes \zeta_c$$

$$(8b) \quad \varphi \cdot \mu_{\mathcal{T}} = \sum_{\gamma \in \Gamma} \alpha_c |\gamma_c(\mathbf{x})| |D\varphi(m_c(\mathbf{x}))| \delta_{\varphi(m_c(\mathbf{x}))} \otimes \zeta_c$$

Define the action of φ on \mathcal{T} by $\varphi \cdot \mathcal{T} = (S, \varphi(\mathbf{x}), \boldsymbol{\alpha}, \boldsymbol{\zeta})$. Then we have

$$(8c) \quad \begin{aligned} \mu_{\varphi \cdot \mathcal{T}} &= \sum_{\gamma \in \Gamma} \alpha_c |\gamma_c(\varphi(\mathbf{x}))| \delta_{m_c(\varphi(\mathbf{x}))} \otimes \zeta_c \\ &\simeq \varphi \cdot \mu_{\mathcal{T}} , \end{aligned}$$

with the approximations $\varphi(m_c(\mathbf{x})) \simeq m_c(\varphi(\mathbf{x}))$ and

$$|D\varphi(m_c(\mathbf{x}))| \simeq \frac{|\gamma_c(\varphi(\mathbf{x}))|}{|\gamma_c(\mathbf{x})|}.$$

3. LDDMM FOR DISCRETE IMAGE VARIFOLDS

At the core of geodesic brain mapping is our norm-distance that we define on the space of varifold-brains. For this we define a family of varifold norms that measure the size of the difference between elements in the space.

3.1. Image-varifold LDDMM. Let K_1 and K_2 be two positive kernels respectively on \mathbb{R}^d and \mathcal{F} . This means that K_1 is defined on $\mathbb{R}^d \times \mathbb{R}^d$ with values in \mathbb{R} such that, for all $n > 0$, all $x_1, \dots, x_n \in \mathbb{R}^d$ and $\lambda_1, \dots, \lambda_n \in \mathbb{R}$, one has

$$\sum_{k,l=1}^n \lambda_k \lambda_l K_1(x_k, x_l) \geq 0.$$

The same condition is assumed for K_2 , replacing \mathbb{R}^d by \mathcal{F} . A natural choice for K_1 , the spatial kernel, is to use radial basis functions (such as Gaussian, or Matérn kernels [2, 39, 11, 19]). Image kernels for categorical features are provided by positive definite matrices with size equal to the number of features, with entries equal to $K_2(f, g)$ for all pairs $f, g \in \mathcal{F}$.

Define the varifold inner product by the condition, holding for all $x, y \in \mathbb{R}^d$ and $f, g \in \mathcal{F}$,

$$(9) \quad \langle \delta_x \otimes \delta_f, \delta_y \otimes \delta_g \rangle_{W^*} = K_1(x, y) K_2(f, g).$$

By linearity, this defines a unique inner product between measures over $\mathbb{R}^d \times \mathcal{F}$. The notation “ W^* ” comes from the fact that this inner product can be interpreted as that associated with the dual space of the reproducing kernel Hilbert space on functions defined on $\mathbb{R}^d \times \mathcal{F}$ associated with the tensor product of K_1 and K_2 . Similarly, for two measures ζ, ζ' on \mathcal{F} , we will write

$$\langle \zeta, \zeta' \rangle_{W_2^*} = \int_{\mathcal{F} \times \mathcal{F}} K_2(f, g) d\zeta(f) d\zeta'(g).$$

Let V be a space of vector fields, i.e., of functions $v : \mathbb{R}^d \rightarrow \mathbb{R}^d$. We assume that V is equipped with an inner product denoted $\langle \cdot, \cdot \rangle_V$ and associated norm $\|\cdot\|_V$ and forms furthermore a Hilbert space so that it is complete for its norm topology. We

also assume that elements in V have at least one continuous derivative, and more precisely that there exists a constant A such that, for any $x \in \mathbb{R}^d$ and any $v \in V$,

$$(10) \quad |v(x)| + |Dv(x)| \leq A\|v\|_V.$$

(Here, we let $|Dv(x)|$ denote any matrix norm applied to the $d \times d$ differential of v .)

The LDDMM (discrete) varifold matching problem is, given two varifolds structures $\mathcal{T}^{(k)} = (S^{(k)}, \mathbf{x}^{(k)}, \boldsymbol{\alpha}^{(k)}, \boldsymbol{\zeta}^{(k)})$, $S^{(k)} = (I^{(k)}, C^{(k)})$, $k = 0, 1$, template and target respectively, the variational problem is:

Variational Problem 1.

$$(11a) \quad \inf_{v(\cdot) \in L^2([0,1],V)} \int_0^1 \|v(t)\|_V^2 dt + \frac{1}{\sigma^2} \|\mu_{\varphi(1) \cdot \mathcal{T}^{(0)}} - \mu_{\mathcal{T}^{(1)}}\|_{W^*}^2$$

$$(11b) \quad \text{with} \quad \partial_t \varphi(t) = v(t) \circ \varphi(t).$$

This formulation follows the common pattern of other LDDMM algorithms [6, 44, 15, 8, 51]. Because the action only affects vertexes, this problem can be reduced using an RKHS argument introduced for the registration of landmarks [20, 15], discrete curves [16] and surfaces [44] with an optimization over point-set trajectories.

More precisely, Eq. (10) implies that V is a reproducing kernel Hilbert space, and because it is a space of vector fields, its kernel K_V is defined on $\mathbb{R}^d \times \mathbb{R}^d$ and takes values in the space of $d \times d$ matrices with real coefficients. This kernel is such that, for any fixed $y \in \mathbb{R}^d$, $a \in \mathbb{R}^d$, (i) the vector field $K_V(\cdot, y)a : x \mapsto K_V(x, y)a$ belongs to V and (ii)

$$\langle K(\cdot, y)a, v \rangle_V = a^T v(y)$$

for all $v \in V$. One can then show that the optimal v takes the form

$$(12) \quad v(t, \cdot) = \sum_{i \in I^{(0)}} K(\cdot, z_i(t)) a_i(t)$$

where $\mathbf{a}(t) = (a_i(t), i \in I^{(0)})$ are free d -dimensional vectors and the d -dimensional points $\mathbf{z}(t) = (z_i(t), i \in I^{(0)})$ are defined in the following reduced problem.

Variational Problem 2.

$$(13a) \quad \inf_{a_i(t), t \in [0,1], i \in I^{(0)}} \sum_{i,j \in I^{(0)}} \int_0^1 a_i(t)^T K(z_i(t), z_j(t)) a_j(t) dt$$

$$(13b) \quad + \frac{1}{\sigma^2} \|\mu_{(S^{(0)}, \mathbf{z}(1), \boldsymbol{\alpha}^{(0)}, \boldsymbol{\zeta}^{(0)})} - \mu_{\mathcal{T}^{(1)}}\|_{W^*}^2$$

with

$$(13c) \quad \partial_t z_i(t) = \sum_{j \in I^{(0)}} K(z_i(t), z_j(t)) a_j(t), \quad z_i(0) = x_i^{(0)}, \quad i \in I^{(0)}.$$

3.2. Gradient of the objective function. The optimization in Variational Problem 2 is with respect to the trajectories $\mathbf{a}(t) = (a_i(t), i \in I^{(0)})$. The optimal diffeomorphism $\varphi(t, \cdot)$ in Eq. (11a) is then given by $\varphi(t, x) = y(t)$ where $y(\cdot)$ solves the ODE:

$$\partial_t y = \sum_{i \in I^{(0)}} K(y(t), z_i(t)) a_i(t)$$

with $y(0) = x$.

The gradient, with respect to $\mathbf{a}(\cdot)$, of the objective function in Eq. (13a) is obtained with the adjoint method and works as follows. Introduce a co-state $\mathbf{p}(\cdot) = (p_i(\cdot), i \in I^{(0)})$. Define the Hamiltonian, evaluated at configurations $\tilde{\mathbf{p}}, \tilde{\mathbf{z}}, \tilde{\mathbf{a}}$ (that do not depend on time):

$$H(\tilde{\mathbf{p}}, \tilde{\mathbf{z}}, \tilde{\mathbf{a}}) = \sum_{i,j \in I^{(0)}} \tilde{p}_i^T K(\tilde{z}_i, \tilde{z}_j) \tilde{a}_j - \sum_{i,j \in I^{(0)}} \tilde{a}_i^T K(\tilde{z}_i, \tilde{z}_j) \tilde{a}_j.$$

Then the gradient is computed in two steps. One first solves the system:

$$(14a) \quad \begin{cases} \partial_t \mathbf{z}(t) = \partial_{\tilde{\mathbf{p}}} H(\mathbf{p}(t), \mathbf{z}(t), \mathbf{a}(t)) \\ \partial_t \mathbf{p}(t) = -\partial_{\tilde{\mathbf{z}}} H(\mathbf{p}(t), \mathbf{z}(t), \mathbf{a}(t)) \end{cases}$$

with boundary conditions $\mathbf{z}(0) = \mathbf{x}^{(0)}$ and:

$$(14b) \quad \mathbf{p}(1) = -\nabla U(\mathbf{z}(1))$$

where

$$(14c) \quad U(\mathbf{x}) = \frac{1}{\sigma^2} \|\mu_{(S^{(0)}, \mathbf{x}, \boldsymbol{\alpha}^{(0)}, \zeta^{(0)})} - \mu_{\mathcal{T}^{(1)}}\|_{W^*}^2.$$

The gradient of the objective function is then given by:

$$t \mapsto -\partial_{\tilde{\mathbf{a}}} H(\mathbf{p}(t), \mathbf{z}(t), \mathbf{a}(t))^T \mathbf{p}(t).$$

The details of this computation have been provided in multiple places (see references above) and the only computation that is specific to our discussion is the evaluation of (14b) on which we now focus.

3.3. Derivative of the data attachment term in 3D and 2D. We now examine both the 3D and 2D cases using similar arguments for the computation of the derivative of U in Eq. (14c). The computation involves the inward weighted inward normal vectors to the faces of the simplices. In 3D, for the tetrahedron $\gamma_c(\mathbf{x}) = \left\{ \sum_{i=0}^3 a_i x_{c_i}, a_i \geq 0, \sum_{i=0}^3 a_i = 1 \right\}$, these vectors are

$$(15) \quad \begin{aligned} n_{c,0} &= -(x_{c_2} - x_{c_1}) \times (x_{c_3} - x_{c_1}) \\ n_{c,1} &= (x_{c_2} - x_{c_0}) \times (x_{c_3} - x_{c_0}) \\ n_{c,2} &= -(x_{c_1} - x_{c_0}) \times (x_{c_3} - x_{c_0}) \\ n_{c,3} &= (x_{c_1} - x_{c_0}) \times (x_{c_2} - x_{c_0}). \end{aligned}$$

In 2D, with tetrahedra replaced by triangles, normals to triangle edges are defined as follow. Letting $J = \begin{pmatrix} 0 & -1 \\ 1 & 0 \end{pmatrix}$, the normals attached to each triangle are

$$(16) \quad \begin{aligned} n_{c,0} &= J(x_{c_2} - x_{c_1}) \\ n_{c,1} &= J(x_{c_0} - x_{c_2}) \\ n_{c,2} &= J(x_{c_1} - x_{c_0}). \end{aligned}$$

Both Eq. (15) and Eq. (16) obey the general definition in which, for $j \geq 1$, $n_{c,j}$ is the unique vector such that

$$(17a) \quad n_{c,j}^T u = (-1)^{j-1} \det \left(u, x_{c_1} - x_{c_0}, \dots, x_{c_{j-1}} - x_{c_0}, x_{c_{j+1}} - x_{c_0}, \dots, x_{c_d} - x_{c_0} \right)$$

for all $u \in \mathbb{R}^d$, and

$$(17b) \quad n_{c,0}^T u = -\det\left(u, x_{c_2} - x_{c_1}, \dots, x_{c_d} - x_{c_1}\right)$$

for all $u \in \mathbb{R}^d$. They furthermore satisfy

$$(17c) \quad \sum_{j=0}^d n_{c,j} = 0.$$

(This property can be easily checked for $d = 2$ or 3 .)

We now calculate the derivative of the data attachment term.

Proposition 1. *Let $S^{(k)} = (I^{(k)}, C^{(k)})$, $k = 0, 1$. then the derivative of U in Eq. (14c) with respect to x_j is*

$$\partial_{x_j} U(\mathbf{x}) = \frac{2}{\sigma^2} \partial_{x_j} \langle \mu_{(S^{(0)}, \mathbf{x}, \boldsymbol{\alpha}^{(0)}, \boldsymbol{\zeta}^{(0)})}, \mu_{(S^{(0)}, \tilde{\mathbf{x}}, \boldsymbol{\alpha}^{(0)}, \boldsymbol{\zeta}^{(0)})} - \mu_{\mathcal{T}^{(1)}} \rangle_{W^*}.$$

evaluated with $\tilde{\mathbf{x}} = \mathbf{x}$, with

$$(18) \quad \partial_{x_j} \langle \mu_{(S, \mathbf{x}, \boldsymbol{\alpha}, \boldsymbol{\zeta})}, \mu_{(S', \mathbf{x}', \boldsymbol{\alpha}', \boldsymbol{\zeta}')} \rangle_{W^*} = \sum_{c \in \mathcal{C}: j \in c} \sum_{c' \in \mathcal{C}'} \alpha_c \alpha_{c'} |\gamma_{c'}(\mathbf{x}')| \langle \zeta_c, \zeta_{c'} \rangle_{W_2^*} \left(\frac{1}{d+1} |\gamma_c(\mathbf{x})| \nabla_1 K_1(m_c(\mathbf{x}), m_{c'}(\mathbf{x}')) + \frac{1}{d!} K_1(m_c(\mathbf{x}), m_{c'}(\mathbf{x}')) n_c(x_j) \right)$$

where $n_c(x_j)$ is the 3D normal to the face opposed to x_j in $\gamma(c)$ of Eqn. (15).

See the appendix for a proof.

4. IMAGE VARIFOLDS AND SPATIAL TRANSCRIPTOMIC DATA.

Spatially resolved transcriptomics probe a large number of targeted mRNA molecules with high-resolution location information [5]. After post-processing, this data can take various forms, for example represented as a 2D image with a large number of channels (associated with the measured gene set), as a list of points in space with attached gene count information (reconstructing single-cell RNAseq information combined with location [48]), or simply as a long list of single mRNA molecules with their detected location. We here consider a general representation that includes most situations of interest. We let \mathcal{G} denote the set of targeted genes, whose size $|\mathcal{G}| = N$ can vary from several hundreds to several thousands.

We assume that the input data is a large family indexing a spatial unit $j \in \mathcal{J}$ associating a location and a list of genes, in the form $y_j, (g_{j,k}, k = 1, \dots, n_j)$, indicating that genes $g_{j,1}, \dots, g_{j,n_j}$ were detected at location y_j (genes in the list may be repeated). A natural representation becomes the number of detections of gene g at location y_j , denoted

$$(y_j, (\nu_j(g), g \in \mathcal{G})) , j \in \mathcal{J} .$$

This representation includes raw spatially resolved transcriptomics data without additional processing with $n_j = 1$ for all j , as well as cell-centered data where y_j is the cell center and the $\nu_j(g)$'s are the gene counts associated with that cell. Preprocessing steps which cluster the raw data can be associated with this representation,

the example we explore being a pre-analysis identifying single cells and cell types [32] (see Section 4.3).

To construct our varifolds $\mu_{\mathcal{T}} = \sum_{c \in C} \alpha_c |\gamma_c(\mathbf{x})| \delta_{m_c(\mathbf{x})} \otimes \zeta_c$ we assume a spatial resolution is given as a length parameter λ in μm defining a regular mesh that is first built within a bounding box containing the data and then pruned by deleting all simplices that contain no point y_j , $j \in \mathcal{J}$. The pruned mesh provides the components (I, C, \mathbf{x}) supporting the image varifold. Our simplicial family $\gamma_c(\mathbf{x})$, $c \in C$ is formed from the vertices, from which we define the image weights and the probability laws (α_c, ζ_c) , $c \in C$ on the functional features. There are alternative choices for these features, listed below, each of them leading to specific definitions of α_c, ζ_c and image kernel K_2 .

4.1. Gene Features. The image weights α_c represent densities (counts per unit volume). There are two options for their definitions, namely the density of detected mRNA molecules, or the density of points y_j , $j \in \mathcal{J}$, which makes sense to consider, e.g., if indexes $j \in \mathcal{J}$ enumerate single cells. In both cases, given that ζ_c is a probability distribution on features which we first take as the genes $\mathcal{F} = \mathcal{G}$ with $f = g \in \mathcal{G}$, we let $\zeta_c(g)$ be the frequency of counts for gene $g \in \mathcal{G}$ relative to all the counts $y_j \in \gamma_c(\mathbf{x})$. This gives:

$$(19) \quad \zeta_c(g) = \frac{\sum_{j: y_j \in \gamma_c(\mathbf{x})} \nu_j(g)}{\sum_{\tilde{g} \in \mathcal{G}} \sum_{j: y_j \in \gamma_c(\mathbf{x})} \nu_j(\tilde{g})}$$

$$\text{with } \begin{cases} \alpha_c = \frac{1}{|\gamma_c(\mathbf{x})|} \sum_{\tilde{g} \in \mathcal{G}} \sum_{j: y_j \in \gamma_c(\mathbf{x})} \nu_j(\tilde{g}), \\ \text{or } \alpha_c = \frac{1}{|\gamma_c(\mathbf{x})|} |\{j : y_j \in \gamma_c(\mathbf{x})\}|. \end{cases}$$

We note that, with the second choice for α_c , one disregards the information provided by the total number of counts in each cell. If one thinks of j as indexing cells in a tissue, the first choice for α_c relates to the number of counts per volume, and the second to the number of cells per volume.

Since \mathcal{G} is a finite set, the image kernel is a positive definite matrix $(K_2(g, \tilde{g}), g, \tilde{g} \in \mathcal{G})$. The simplest choice for it is to use the identity, i.e., $K_2(g, \tilde{g}) = 1$ if $g = \tilde{g}$ and 0 otherwise.

Note that, in this section and in the next one, the set \mathcal{G} may be replaced by a representative subset (gene panel) without any change to the discussion.

4.2. RNA Count Features. Define the RNA count space to be features $\mathcal{F} = [0, +\infty)^{\mathcal{G}}$, that is, the set of all families $f = (f(g), g \in \mathcal{G})$ with $f(g) \geq 0$. In this context, the simplest choice is to let ζ_c be a Dirac measure at the averaged counts with mRNA count density:

$$(20) \quad \zeta_c = \delta_{\bar{\nu}_c}, \quad \bar{\nu}_c(g) = \frac{\sum_{j: y_j \in \gamma_c(\mathbf{x})} \nu_j(g)}{|\{j : y_j \in \gamma_c(\mathbf{x})\}|},$$

$$\text{with } \alpha_c = \frac{1}{|\gamma_c(\mathbf{x})|} |\{j : y_j \in \gamma_c(\mathbf{x})\}|.$$

There is a wide range of possible choices for the image kernel K_2 , since we are working with quantitative data. The Gaussian kernel $K_2(\nu, \nu') = \exp(-|\nu - \nu'|^2 / 2\sigma^2)$ is

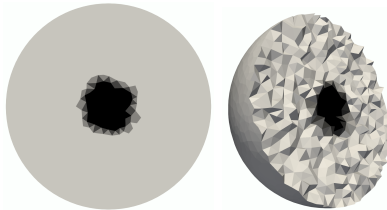


FIGURE 1. Targets for evolutions in Fig. 2 and Fig. 3. (The 3D shape is clipped to show interior data.)

a standard example. For our experiments in the next section, we use the product of a Euclidean and a Cauchy kernels, namely

$$(21) \quad K_2(\nu, \nu') = \frac{\nu^T \nu'}{\sigma^2 + |\nu - \nu'|^2}.$$

Note that, since elements of \mathcal{F} are non-negative, the kernel K_2 can be computed in log scale, i.e., applied to $\log(1 + \nu), \log(1 + \nu')$ instead of ν, ν' .

4.3. Cell Label Features. Now examine the features to be cell types where we assume that the input data has been preprocessed to return cell type labels. We let $\mathcal{F} = \{\ell_1, \dots, \ell_p\}$, the label set, and assume that the data is a list (y_j, L_j) for locations and labels for $j \in \mathcal{J}$. The measure ζ_c can be defined as

$$(22) \quad \zeta_c(\ell_k) = \frac{|\{j : y_j \in \gamma_c(\mathbf{x}), L_j = \ell_k\}|}{|\{j : y_j \in \gamma_c(\mathbf{x})\}|}$$

with $\alpha_c = \frac{1}{|\gamma_c(\mathbf{x})|} |\{j : y_j \in \gamma_c(\mathbf{x})\}|.$

It is natural to use a kernel for which labels are orthogonal, i.e., $K_2(\ell, \tilde{\ell}) = 1$ if $\ell = \tilde{\ell}$ and 0 otherwise for $\ell, \tilde{\ell} \in \mathcal{F}$.

5. EXAMPLES

5.1. A toy example. As a first example, we consider two shapes, supported by discs in 2D or balls in 3D with 2D image feature that can be interpreted as the concentration (between 0 and 1) of some molecule in a substrate. A small disc/ball is compared to a larger one, with the molecule, concentrated in the center, occupying a larger volume in the small shape than in the large one. The registration must therefore globally expand the shape while locally contracting the region occupied by the molecule. This is illustrated in Fig. 2 and Fig. 3. The 2D disc has 0.8K vertexes and 1.5K triangles and the 3D ball has 4K vertexes and 20K tetrahedra.

5.2. MERFISH image registration. We illustrate the previous discussion with preliminary based on MERFISH images of mouse brains [53]. Two-dimensional MERFISH datasets were discretized on grids with spatial resolution $\lambda = 100 \mu\text{m}$. Out of the 700 genes provided for the image, a subset of 10 genes with largest standard deviation was selected to build the image varifolds. We used a Gaussian kernel for K_1 and the kernel provided in Eq. (21) for K_2 after switching to log scale. Figure 4 provides images from two brain sections from the same mouse, the first one being used as template and the second as the target for registration. The top row shows the template, the middle row the target, with the bottom row showing

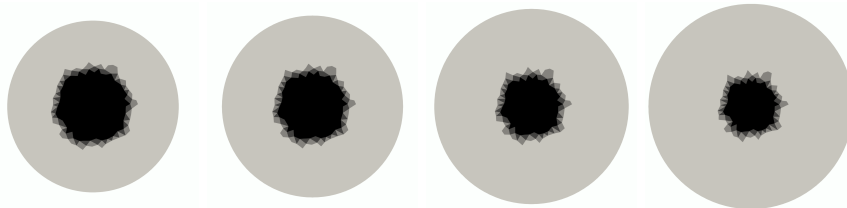


FIGURE 2. Toy example: 2D. Evolution at times $t = 0.0$, $t = 0.3$, $t = 0.7$ and $t = 1.0$. The final image should be compared with the target in Fig. 1.

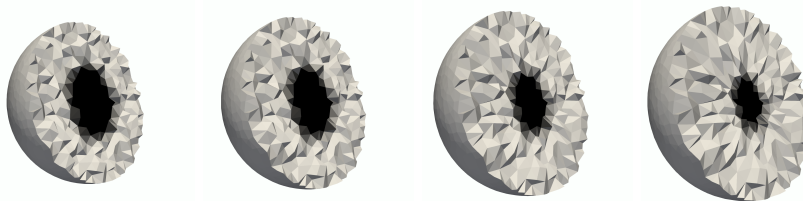


FIGURE 3. Toy example: 3D. Evolution at times $t = 0.0$, $t = 0.3$, $t = 0.7$ and $t = 1.0$. The final image should be compared with the target in Fig. 1. (Shapes are clipped to show interior data.)

the deformed template sections aligned to the target images. Figure 5 shows similar results with much great deformations for the same template (top row) but mapped to a second mouse section (middle row) with the resulting deformed template shown (bottom row). The deformation grids are shown in Fig. 6. We see small deformation when registering the first two sections which come from the same brain and are quite similar, and much stronger changes for the alignment of the first and third sections, which come from different mice and have significant discrepancies.

6. ATLASING: CROSSING MODALITY AND SCALE

6.1. Variational problems. Transferring genomic, cellular and histological data to atlas coordinates is one of the mainstream examples of crossing modalities and crossing scale. Atlases (Fig. 7) are by definition often “cartoons” [33] which make sense at the millimeter tissue scales but are used to interpret the finest molecular and particle scales. Similarly our work in human digital pathology brings histological micron scale of markers together with the atlas scales of Mai-Paxinos (Fig. 8). We associate to the atlas the features space of cartoon labels \mathcal{L} . We want to map the high-resolution gene features with associated probabilities ζ' on \mathcal{F} , the set of micro-scale functional features representing genomic expression or particle identity, to the tissue scale where we only have the cartoon labels.

We assume that the varifolds are represented on meshes, as described in Section 2.3; the micro-scale fine varifold has $\mathcal{T}' = (S', \mathbf{x}', \alpha', \zeta')$, $S' = (I', C')$, with

$$\mu_{\mathcal{T}'} = \sum_{c' \in C'} \alpha'_{c'} |\gamma_{c'}(\mathbf{x}')| \delta_{m_{c'}(\mathbf{x}')} \otimes \zeta'_{c'}.$$

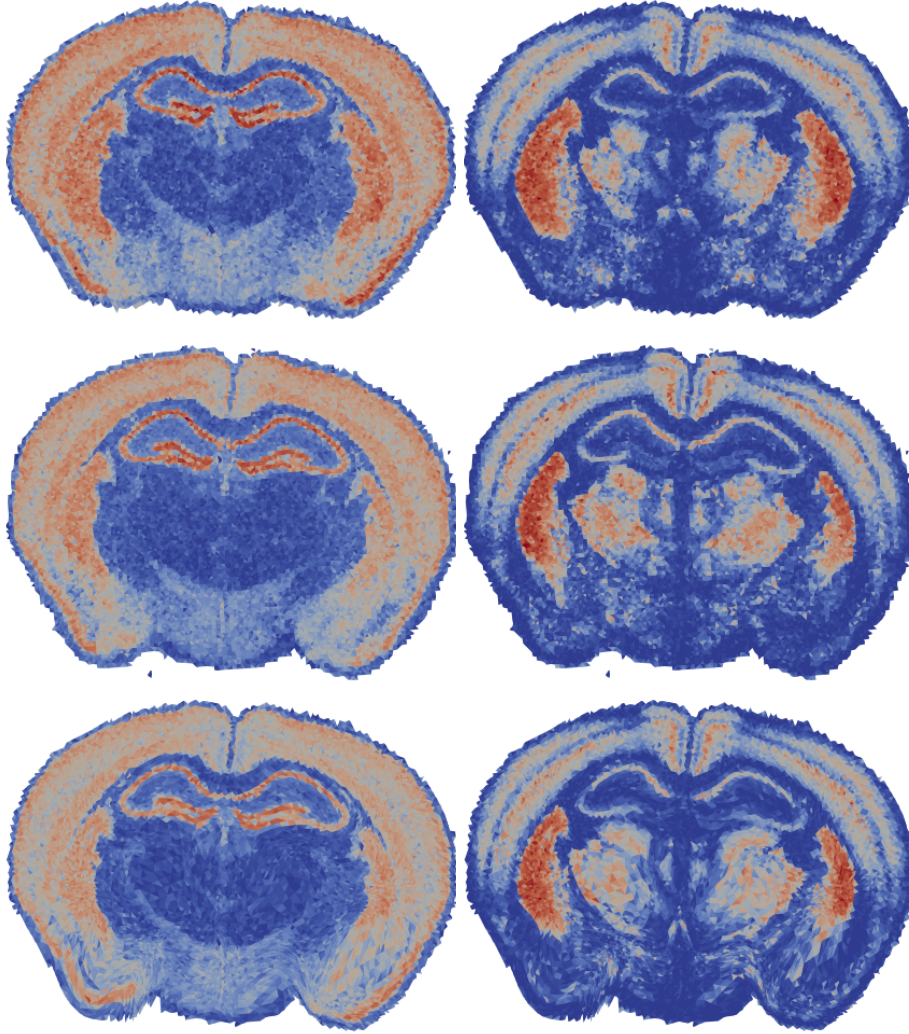


FIGURE 4. MERFish images: Top row shows template with two genes provided by *Atp6ap1* and *Satb2* gene counts (in log scale); middle row shows the target. Bottom row shows the template (top) mapped to the target (middle). Data from [53].

At the coarse tissue scales, we assume that \mathcal{L} is a small set of region labels forming the atlas features, $|\mathcal{L}| \ll |\mathcal{F}|$. The atlas is represented as a varifold defined on a mesh $\mathcal{T} = (S, \mathbf{x}, \boldsymbol{\alpha}, \boldsymbol{\zeta})$, $S = (I, C)$ with $\zeta_c, c \in C$ the atlas feature probability assigning probability to regions. The weights in $\boldsymbol{\alpha} = (\alpha_c, c \in C)$ are unknown, since they are generally not provided in atlases, but we will assume in the following that they are subject to box constraints in the form $\alpha_c^{\min} \leq \alpha_c \leq \alpha_c^{\max}$ for all $c \in C$, where α_c^{\min} and α_c^{\max} are known and correspond to prior expectation on the density of molecules or cells. Note that $\alpha_c^{\min} = 0$ and $\alpha_c^{\max} = \infty$ are allowed, and also $\alpha_c^{\min} = \alpha_c^{\max}$, yielding equality constraints, in case the densities are specified

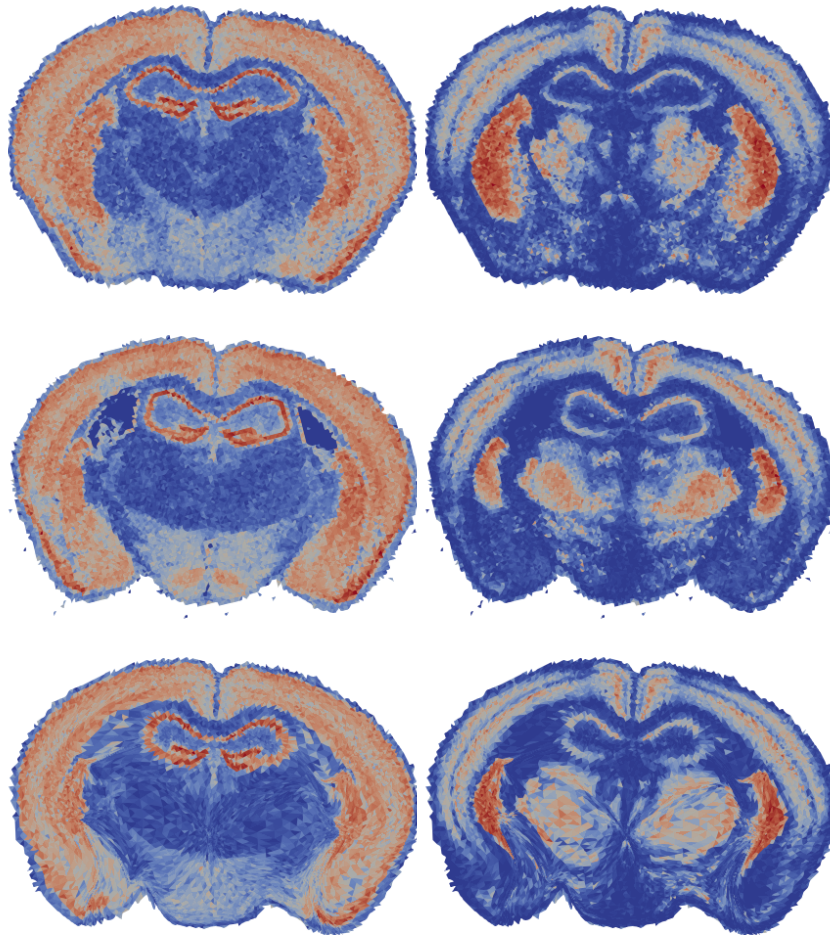


FIGURE 5. Top row shows template with two genes provided by *Atp6ap11* and *Satb2* gene counts (identical to top row Figure 4); middle row shows target of a second mouse with the two genes *Atp6ap11* and *Satb2* gene counts (in log scale); bottom row shows the template (top row previous figure 4) mapped based on a total of 10 genes of highest variance to the second mouse target. Data taken from [53].

or estimated separately. Through the measures ζ_c , we allow for the specification of a probabilistic atlas, and “cartoon representations” (piecewise constant images) are such that simplexes in the same region all have the same probability ζ_c which is a Dirac.

Each category $\ell \in \mathcal{L}$ has a specific expression pattern in the tissue, that we represent by a probability distribution on \mathcal{F} . Since this genomic measure feature is not generally available, we propose to estimate it from data, and introduce a family of parametric measures $(\pi_\vartheta, \vartheta \in \Theta)$ on \mathcal{F} (see examples below). To each label $\ell \in \mathcal{L}$ is associated a parameter $\theta_\ell \in \Theta$ that need to be estimated. The problem

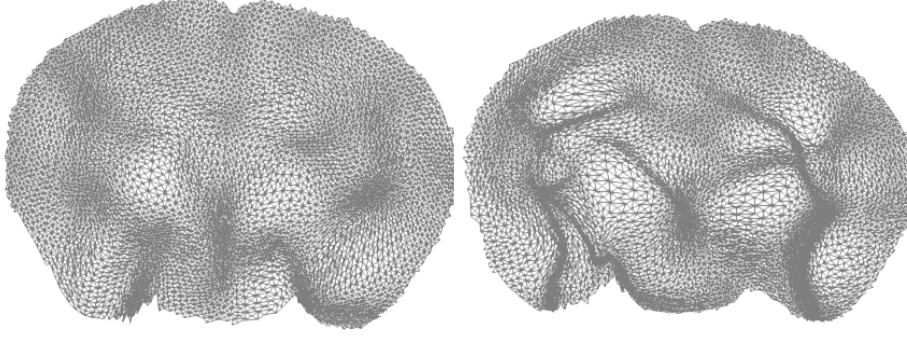


FIGURE 6. Deformation grids for the two mappings shown above, Figures Fig. 4, Fig. 5. Data from [53].

then becomes to simultaneously estimate the diffeomorphism φ of \mathbb{R}^d mapping the atlas to the micro-scale varifold, the parametrization vector $\theta = (\theta_\ell, \ell \in \mathcal{L})$, and the region weights. Importantly, we do not assume that the π_θ 's are probabilities measures, and we interpret $\pi_{\theta_\ell}(\mathcal{F})$ as a measure of the density of molecules or cells with label ℓ . Using this model, the imputed gene or cellular density at each site $c \in C$ becomes $\alpha_c = \sum_{\ell \in \mathcal{L}} \zeta_c(\ell) \pi_{\theta_\ell}(\mathcal{F})$ and the probability law at each site $c \in C$ is $\sum_{\ell \in \mathcal{L}} \zeta_c(\ell) \pi_{\theta_\ell} / \alpha_c$, yielding a varifold representation of the atlas (with imputed gene or cellular features)

$$\mu_{\mathcal{T}}^\theta = \sum_{c \in C} |\gamma_c(\mathbf{x})| \delta_{m_c(\mathbf{x})} \otimes \left(\sum_{\ell \in \mathcal{L}} \zeta_c(\ell) \pi_{\theta_\ell} \right).$$

The mapping problem is to map $\mu_{\varphi(1)\cdot\mathcal{T}}^\theta$ close to $\mu_{\mathcal{T}'}$, with φ acting on meshes as defined in Section 2.3. This estimation is performed using alternating minimization, looping over the estimation of φ with fixed θ and the estimation of θ with fixed φ minimizing $\|\mu_{\varphi(1)\cdot\mathcal{T}}^\theta - \mu_{\mathcal{T}'}\|_{W^*}^2$ with our variational problem for crossing scales.

Variational Problem 3.

$$(23) \quad \inf_{\theta_\ell, \ell \in \mathcal{L}, v(\cdot) \in L^2([0,1], V)} \int_0^1 \|v(t)\|_V^2 dt + \frac{1}{\sigma^2} \|\mu_{\varphi(1)\cdot\mathcal{T}}^\theta - \mu_{\mathcal{T}'}\|_{W^*}^2$$

with $\partial_t \varphi(t) = v(t) \circ \varphi(t)$

and $\alpha_c^{\min} \leq \sum_{\ell \in \mathcal{L}} \zeta_c(\ell) \pi_{\theta_\ell}(\mathcal{F}) \leq \alpha_c^{\max}, c \in C.$

Fixing $v(\cdot) \in L^2[0, 1]$, with varifold norm kernel a product form (9), $K = K_1 K_2$, then we have:

$$(24) \quad \|\mu_{\varphi(1)\cdot\mathcal{T}}^\theta - \mu_{\mathcal{T}'}\|_{W^*}^2 =$$

$$\sum_{c_0, c_1 \in C} \sum_{\ell_0, \ell_1 \in \mathcal{L}} |\gamma_{c_0}| \gamma_{c_1} |\zeta_{c_0}(\ell_0) \zeta_{c_1}(\ell_1) K_1(m_{c_0}, m_{c_1}) \int_{\mathcal{F}^2} K_2(f_0, f_1) d\pi_{\theta_{\ell_0}}(f_0) d\pi_{\theta_{\ell_1}}(f_1)$$

$$- 2 \sum_{c \in C, c' \in C'} \sum_{\ell \in \mathcal{L}} \alpha'_{c'} |\gamma_c| |\gamma'_{c'}| \zeta_c(\ell) K_1(m_c, m'_{c'}) \int_{\mathcal{F}^2} K_2(f, f') d\pi_{\theta_\ell}(f) d\zeta'_{c'}(f'),$$

where we have denoted for short $\gamma_c = \gamma_c(\varphi(1) \cdot \mathbf{x})$, $m_c = m_c(\varphi(1) \cdot \mathbf{x})$, $\gamma'_{c'} = \gamma_{c'}(\mathbf{x}')$, $m'_{c'} = m_{c'}(\mathbf{x}')$.

6.2. Special cases. Equation (24) must be minimized in θ subject to the density constraints in Eq. (23). This generally provides a nonlinear programming problem. However, in some special cases, including those listed below, this problem boils down to quadratic programming (QP).

Example 1. Take cell types as micro-scale features, so that $(\zeta'_{c'}(f), f \in \mathcal{F})$ are the probabilities on each cell type. Let Θ be the space of positive measures on \mathcal{F} , taking $\pi_\theta(f) = \theta(f)$, $\theta(f) \geq 0$, $f \in \mathcal{F}$.

Our problem is to estimate the density of each cell type in every region $\theta_\ell(f)$, $f \in \mathcal{F}$, $\ell \in \mathcal{L}$. Choosing the identity kernel on \mathcal{F} , with $K_2(f, \tilde{f}) = 1$ if $f = \tilde{f}$ and 0 otherwise, the minimization of Eq. (24) reduces to:

$$\begin{aligned} & \inf_{\substack{\theta_\ell, \ell \in \mathcal{L} \\ \theta_\ell(f) \geq 0, f \in \mathcal{F}}} \sum_{c_0, c_1 \in C} \sum_{\ell_0, \ell_1 \in \mathcal{L}} |\gamma_{c_0}| |\gamma_{c_1}| \zeta_{c_0}(\ell_0) \zeta_{c_1}(\ell_1) K_1(m_{c_0}, m_{c_1}) \sum_{f \in \mathcal{F}} \theta_{\ell_0}(f) \theta_{\ell_1}(f) \\ & - 2 \sum_{c \in C, c' \in C'} \sum_{\ell_0 \in \mathcal{L}} \alpha'_{c'} |\gamma_c| |\gamma'_{c'}| \zeta_c(\ell_0) K_1(m_c, m'_{c'}) \sum_{f \in \mathcal{F}} \theta_{\ell_0}(f) \zeta'_{c'}(f), \end{aligned}$$

with constraints

$$\alpha_c^{\min} \leq \sum_{\ell \in \mathcal{L}} \sum_{f \in \mathcal{F}} \zeta_c(\ell) \theta_\ell(f) \leq \alpha_c^{\max}, c \in C.$$

Example 2. Now consider mRNA counts on genes in \mathcal{G} . Take a simple model where parameters are $\theta = (\theta(g), g \in \mathcal{G}) \in [0, +\infty)^{\mathcal{G}}$ with $\pi_\theta = w_\theta \delta_{\eta_\theta}$, a weighted Dirac measure, taking $w_\theta = \sum_{g \in \mathcal{G}} \theta(g)$ and $\eta_\theta(g) = \theta(g)/w_\theta$. So, to each label ℓ is assigned an expression vector θ_ℓ with w_{θ_ℓ} representing the total expression and η_{θ_ℓ} a normalized expression. Taking the kernel as Euclidean on \mathcal{F} (see remark below), $K_2(f, \tilde{f}) = \sum_{g \in \mathcal{G}} f(g) \tilde{f}(g)$, we have

$$\int_{\mathcal{F}} K_2(f, f') d\pi_{\theta_{\ell_0}}(f) d\zeta'_{c'}(f) = \sum_{g \in \mathcal{G}} w_{\theta_{\ell_0}} \eta_{\theta_{\ell_0}}(g) \bar{\theta}_{c'}(g) = \sum_{g \in \mathcal{G}} \theta_{\ell_0}(g) \bar{\theta}_{c'}(g)$$

where $\bar{\theta}_{c'}$ is the average expression $\int_{\mathcal{F}} f d\zeta'_{c'}(f)$. This gives the minimization of Eq. (24) reducing to:

$$\begin{aligned} & \inf_{\substack{\theta_\ell, \ell \in \mathcal{L} \\ \theta_\ell(g) \geq 0, g \in \mathcal{G}}} \sum_{c_0, c_1 \in C} \sum_{\ell_0, \ell_1 \in \mathcal{L}} |\gamma_{c_0}| |\gamma_{c_1}| \zeta_{c_0}(\ell_0) \zeta_{c_1}(\ell_1) K_1(m_{c_0}, m_{c_1}) \sum_{g \in \mathcal{G}} \theta_{\ell_0}(g) \theta_{\ell_1}(g) \\ & - 2 \sum_{c \in C, c' \in C'} \sum_{\ell_0 \in \mathcal{L}} \alpha'_{c'} |\gamma_c| |\gamma'_{c'}| \zeta_c(\ell_0) K_1(m_c, m'_{c'}) \sum_{g \in \mathcal{G}} \theta_{\ell_0}(g) \bar{\theta}_{c'}(g) \end{aligned}$$

with constraints

$$\alpha_c^{\min} \leq \sum_{\ell \in \mathcal{L}} \sum_{g \in \mathcal{G}} \zeta_c(\ell) \theta_\ell(g) \leq \alpha_c^{\max}, c \in C.$$

Even though they were obtained from different models and contexts, the two examples above simplify to almost identical QP problems, respectively in $(\theta_\ell, \ell \in \mathcal{L})$. These problems are rephrased explicitly as QP problems below.

Algorithm 1. For Example 1., let $K_2(f, \tilde{f}) = 1$ if $f = \tilde{f}$ and 0 otherwise, defining

$$(25) \quad \begin{cases} A_{\ell_0, \ell_1} = \sum_{c_0, c_1 \in C} \alpha_{c_0} \alpha_{c_1} |\gamma_{c_0}| |\gamma_{c_1}| \zeta_{c_0}(\ell_0) \zeta_{c_1}(\ell_1) K_1(m_{c_0}, m_{c_1}) \\ b_{\ell_0}(f) = \sum_{c \in C, c' \in C'} \alpha_c \alpha'_{c'} |\gamma_c| |\gamma'_{c'}| \zeta_c(\ell_0) K_1(m_c, m'_{c'}) \zeta'_{c'}(f), \end{cases}$$

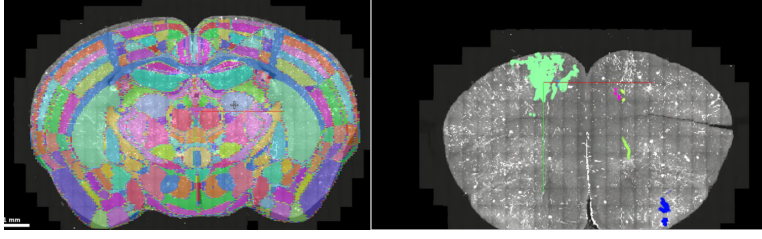


FIGURE 7. Depicting Allen Atlas scale (left) and mouse micro scales right.

then $(\theta_\ell, \ell \in \mathcal{L})$ minimizes

$$(26) \quad \begin{aligned} \Phi_1(\theta) &= \sum_{\ell_0, \ell_1 \in \mathcal{F}} \sum_{f \in \mathcal{F}} A_{\ell_0, \ell_1} \theta_{\ell_0}(f) \theta_{\ell_1}(f) - 2 \sum_{\ell_0 \in \mathcal{L}} \sum_{f \in \mathcal{F}} b_{\ell_0}(f) \theta_{\ell_0}(f) \\ &\text{subject to the constraints } \alpha_c^{\min} \leq \sum_{\ell \in \mathcal{L}} \sum_{f \in \mathcal{F}} \zeta_c(\ell) \theta_\ell(f) \leq \alpha_c^{\max}, c \in C. \end{aligned}$$

Algorithm 2. For Example 2., let $K_2(f, \tilde{f}) = \sum_{g \in \mathcal{G}} f(g) \tilde{f}(g)$, $\bar{\theta}_{c'} = \int_{\mathcal{F}} f d\zeta_{c'}$, taking A as in Eq. (25), and define

$$(27) \quad b_{\ell_0}(g) = \sum_{c \in C, c' \in C'} \alpha_c \alpha_{c'} |\gamma_c| |\gamma_{c'}| \zeta_c(\ell_0) K_1(m_c, m'_{c'}) \bar{\theta}_{c'},$$

then $(\theta_\ell, \ell \in \mathcal{L})$ minimizes

$$(28) \quad \begin{aligned} \Phi_2(\theta) &= \sum_{\ell_0, \ell_1 \in \mathcal{L}} \sum_{g \in \mathcal{G}} A_{\ell_0, \ell_1} \theta_{\ell_0}(g) \theta_{\ell_1}(g) - 2 \sum_{\ell_0 \in \mathcal{L}} \sum_{g \in \mathcal{G}} b_{\ell_0}(g) \theta_{\ell_0}(g) \\ &\text{subject to the constraints } \alpha_c^{\min} \leq \sum_{\ell \in \mathcal{L}} \sum_{g \in \mathcal{G}} \zeta_c(\ell) \theta_\ell(g) \leq \alpha_c^{\max}, c \in C. \end{aligned}$$

Remark 3. The Euclidean kernel used for K_2 in Example 2 is degenerate, in the sense that it induces a finite-dimensional RKHS, which can be identified to $\mathbb{R}^{\mathcal{G}}$ with the standard Euclidean norm. In this representation, probability measures on \mathcal{F} are identified with their expectations, so that the metric does not differentiate between a Dirac measure δ_f and a probability measure ζ with expectation f . This explains why, in this example, the measures $\zeta'_{c'}$ were replaced with their associated average expression.

If K_1 is a spatial kernel, the product RKHS associated with $K_1 K_2$ is identical to the RKHS of multivariate functions $x \mapsto F(x) \in \mathbb{R}^{\mathcal{G}}$, formed with the $|\mathcal{G}|$ -fold tensor product of scalar RKHS's associated with K_1 . Image varifolds associated with a Euclidean image kernel are therefore identified to $|\mathcal{G}|$ -dimensional vector measures.

7. POINT PROCESSES AND IMAGE VARIFOLD

The realizations of a compound point process \mathcal{N} are discrete image varifolds

$$\mathcal{N} = \sum_{k=1}^n \delta_{x_k} \otimes \delta_{f_k}.$$

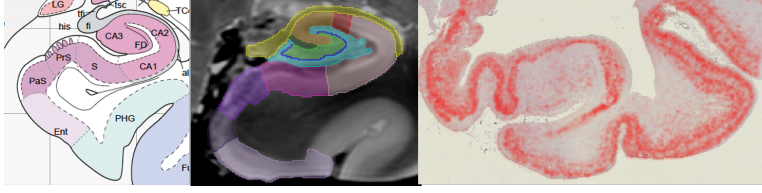


FIGURE 8. Mai-Paxinos atlas section and high field MRI with Tau molecular pathology (right).

Their distributions are specified by a non-negative intensity function λ defined on \mathbb{R}^d and a transition probability $(x, f) \mapsto \zeta(x, f)$ defined on $\mathbb{R}^d \times \mathcal{F}$ (so that $\zeta(x, \cdot)$ is for all x a probability on \mathcal{F}), such that

- (i) for $\Omega \subset \mathbb{R}^d$ and $A \subset \mathcal{F}$, $\mathbf{N}(\Omega \times A)$ follows a a Poisson distribution with parameter

$$\Lambda^{\mathbf{N}}(\Omega \times A) = \int_{\Omega} \lambda(x) \zeta(x, A) dx.$$

- (ii) $\mathbf{N}(\Omega \times A)$ is independent of $\mathbf{N}(\Omega' \times A')$ if $(\Omega \times A) \cap (\Omega' \times A') = \emptyset$.

In the following we will make the abuse of notation $N(\Omega) = N(\Omega \times \mathcal{F})$ for the total number of points in Ω and similarly write $\Lambda^{\mathbf{N}}(\Omega) = \Lambda^{\mathbf{N}}(\Omega \times \mathcal{F})$. We assume that λ is compactly supported, which allows us to represent realizations of \mathbf{N} as finite sums.

If F is a function on $\mathbb{R}^d \times \mathcal{F}$, its pairing with N is

$$(N|F) = \sum_{k=1}^n F(x_k, f_k).$$

The conditional expectation of $(N|F)$ given the point set n, x_1, \dots, x_n is

$$E((N|F)|n, x_1, \dots, x_n) = \sum_{k=1}^n \int_{\mathcal{F}} F(x_k, f) d\zeta(x_k, f)$$

which is the pairing of F with the varifold $\sum_{k=1}^n \delta_{x_k} \otimes \zeta(x_k, \cdot)$. One also has

$$E((N|F)) = \int_{\mathbb{R}^d} \int_{\mathcal{F}} F(x, f) d\zeta(x, f) \lambda(x) dx$$

therefore associated with the varifold $\mu_{\mathbf{N}} = \lambda \otimes \zeta$. We will write $\mathbf{N} \sim \text{cpp}(\lambda, \zeta)$ to indicate that \mathbf{N} is a compound Poisson point process with intensity λ and transition probability ζ .

If $\mathbf{N} = \text{cpp}(\lambda, \zeta)$ and φ is a diffeomorphism, we define $\varphi \cdot \mathbf{N} := \text{cpp}(\lambda \circ \varphi^{-1}, \zeta(\varphi^{-1}(\cdot), \cdot))$, so that

$$\begin{aligned} (\mu_{\varphi \cdot \mathbf{N}}|F) &= \int_{\mathbb{R}^d} \int_{\mathcal{F}} F(x, f) d\zeta(\varphi^{-1}(x), f) \lambda(\varphi^{-1}(x)) dx \\ &= \int_{\mathbb{R}^d} \int_{\mathcal{F}} |d\varphi(x)| F(\varphi(x), f) d\zeta(x, f) \lambda(x) dx \\ &= (\varphi \cdot \mu_{\mathbf{N}}|F). \end{aligned}$$

We now design a test statistic to assess whether the observations N_1, N_2 of two independent compound Poisson processes result from $\mathbf{N}_1 = \varphi_1 \cdot \mathbf{N}$ and $\mathbf{N}_2 = \varphi_2 \cdot \mathbf{N}$, where $\mathbf{N} = \text{cpp}(\lambda, \zeta)$ and φ_1 and φ_2 are diffeomorphisms. (\mathbf{N} is therefore

a “template” compound Poisson process.) We here assume that φ_1 and φ_2 are known, and ignore the bias resulting from the fact that they have possibly been estimated using a registration procedure also involving N_1 and N_2 .

Fix subsets $\Omega \subset \mathbb{R}^d$ and $A \subset \mathcal{F}$, and assume that λ and ζ take constant values, $\bar{\lambda}$ and $\bar{\zeta}$ on Ω (so that $\bar{\lambda}$ is a non-negative number and $\bar{\zeta}$ is a measure on \mathcal{F}). One then has

$$\Lambda^{\mathbf{N}}(\Omega \times A) = \int_{\Omega} \lambda(x) \zeta(x, A) dx = \bar{\lambda} \bar{\zeta}(A) |\Omega|$$

and, under the assumptions above:

$$\Lambda^{\mathbf{N}_i}(\Omega_i \times A) = \Lambda^{\mathbf{N}}(\Omega \times A) \frac{|\Omega_i|}{|\Omega|} = \Lambda^{\mathbf{N}}(\Omega \times A) \chi_i, \quad i = 1, 2,$$

with $\Omega_i = \varphi_i(\Omega)$ and $\chi_i = |\Omega_i|/|\Omega|$. So, the null hypothesis is, for given Ω, A :

$$H_0(\Omega, A) : \frac{\Lambda^{\mathbf{N}_1}(\Omega_1 \times A)}{\chi_1} = \frac{\Lambda^{\mathbf{N}_2}(\Omega_2 \times A)}{\chi_2},$$

and the alternative hypothesis is

$$H_1(\Omega, A) : \frac{\Lambda^{\mathbf{N}_1}(\Omega_1 \times A)}{\chi_1} \neq \frac{\Lambda^{\mathbf{N}_2}(\Omega_2 \times A)}{\chi_2}.$$

We will use the likelihood ratio test statistic to compare the two hypotheses. Letting $\hat{p} = N_1(\Omega_1 \times A)/(N_1(\Omega_1 \times A) + N_2(\Omega_2 \times A))$ and $p = \chi_1/(\chi_1 + \chi_2)$, it is given by

$$(29) \quad T(\Omega, A) = (N_1(\Omega_1 \times A) + N_2(\Omega_2 \times A)) D(\pi_{\hat{p}} || \pi_p),$$

$$\text{with } D(\pi_{\hat{p}} || \pi_p) = \left(\hat{p} \log \frac{\hat{p}}{p} + (1 - \hat{p}) \log \frac{1 - \hat{p}}{1 - p} \right)$$

This test statistic can be computed over partitions $(\Omega_c, c \in C)$ of the support of λ (small enough to justify the constancy assumption). If one takes $A = \mathcal{F}$, the collection $T(\Omega_c, \mathcal{F})$ focus on point density only. Using in addition a partition (A_1, \dots, A_m) of \mathcal{F} (obtained, for example, as clusters interpreted as cell types), we obtain a complete family of statistics $T(\Omega_c, A_j)$ that provides a high-dimensional analysis of the differences between the observed realizations.

8. DISCUSSION

The family of algorithms presented here provides the basis for future mapping technologies that allow for the representation of massive lists of molecular and cellular descriptions of the human body with the tissue scales of radiological and pathological imaging. Unifying the molecular and image scales represents an important step forward in brain mapping. The central representation is the brain as a varifold measure defined on the direct product of space and function.

The algorithms described allow for the molecular computational anatomy mapping program to continue in the vein of D’Arcy Thompson, computing normed distances between brains. A basic principle calculates similarity by acting diffeomorphisms which transforms one brain onto the other measuring the size of the transformation. Central to the theory proposed here is the action which we describe as “copy and paste,” preserving the density of the quantized objects as space is transformed. This emphasizes the representation as containing two objects, the density ρ on \mathbb{R}^d and the field of conditional distributions $(\zeta_x, x \in \mathbb{R}^d)$ representing

function over space. The varifolds norms introduced for placing the varifold measures of brain space into a normed-space score both the density measure as well as function measure.

The varifold brainspace represents both space and function. Because the transformations defined act on space, the variation of the norm with respect to the group action becomes the variation of space through the varifold space kernel weighted by the direct inner product measuring alignment of the function measures.

Interestingly the varifold action we derive makes the molecular scale representation consistent with the tissue scale representation associated to MRI imaging and atlasing at 100 micron - 1 millimeter scale. We explicitly define several features including RNA and cell-centered features. In all the cases the features are represented as empirical probability laws over the RNA or cell identity feature spaces.

As part of the atlasing method we examine several algorithms for transferring the high resolution gene features to the atlas tissue scales by inferring the gene features. We demonstrate that this carries us into a family of quadratic programming problems in which the imputed feature laws are constrained to be probability measures.

We also examine the family of optimal test statistics for the spatial transcriptomic setting and show that the Kullback-Lieber divergence plays a central role in characterizing discriminability. The KL-distance is calculated between the empirical feature laws $\zeta_x, x \in \mathbb{R}^d$ under different hypotheses for the brain measures.

APPENDIX A. PROOF OF PROPOSITION 1

We repeat the statement of the proposition for convenience.

Proposition. *Let $S^{(k)} = (I^{(k)}, C^{(k)})$, $k = 0, 1$. then the derivative of U in Eq. (14c) with respect to x_j is*

$$\partial_{x_j} U(\mathbf{x}) = \frac{2}{\sigma^2} \partial_{x_j} \langle \mu_{(S^{(0)}, \mathbf{x}, \boldsymbol{\alpha}^{(0)}, \boldsymbol{\zeta}^{(0)})}, \mu_{(S^{(0)}, \tilde{\mathbf{x}}, \boldsymbol{\alpha}^{(0)}, \boldsymbol{\zeta}^{(0)})} - \mu_{\mathcal{T}^{(1)}} \rangle_{W^*}.$$

evaluated with $\tilde{\mathbf{x}} = \mathbf{x}$, with

$$(30) \quad \partial_{x_j} \langle \mu_{(S, \mathbf{x}, \boldsymbol{\alpha}, \boldsymbol{\zeta})}, \mu_{(S', \mathbf{x}', \boldsymbol{\alpha}', \boldsymbol{\zeta}')} \rangle_{W^*} = \sum_{c \in C: j \in c} \sum_{c' \in C'} \alpha_c \alpha_{c'} |\gamma_{c'}(\mathbf{x}')| \langle \zeta_c, \zeta_{c'} \rangle_{W_2^*} \left(\frac{1}{d+1} |\gamma_c(\mathbf{x})| \nabla_1 K_1(m_c(\mathbf{x}), m_{c'}(\mathbf{x}')) + \frac{1}{d!} K_1(m_c(\mathbf{x}), m_{c'}(\mathbf{x}')) n_c(x_j) \right)$$

where $n_c(x_j)$ is the 3D normal to the face opposed to x_j in $\gamma(c)$ of Eqn. (15).

Proof. We compute the variation of $\langle \mu_{(S, \mathbf{x}, \boldsymbol{\alpha}, \boldsymbol{\zeta})}, \mu_{(S', \mathbf{x}', \boldsymbol{\alpha}', \boldsymbol{\zeta}')} \rangle_{W^*}$ with respect to a perturbation $\mathbf{h} = (h_i, i \in I)$ on the vertices \mathbf{x} at $\varepsilon = 0$ of the variation:

$$\begin{aligned} & \partial_\varepsilon \langle \mu_{(S, \mathbf{x} + \varepsilon \mathbf{h}, \boldsymbol{\alpha}, \boldsymbol{\zeta})}, \mu_{(S', \mathbf{x}', \boldsymbol{\alpha}', \boldsymbol{\zeta}')} \rangle_{W^*} \Big|_{\varepsilon=0} \\ &= \partial_\varepsilon \left(\sum_{c \in C, c' \in C'} \alpha_c \alpha_{c'} |\gamma_c(\mathbf{x} + \varepsilon \mathbf{h})| |\gamma_{c'}(\mathbf{x}')| \langle \zeta_c, \zeta_{c'} \rangle_{W_2^*} K_1(m_c(\mathbf{x} + \varepsilon \mathbf{h}), m_{c'}(\mathbf{x}')) \right) \Big|_{\varepsilon=0}. \end{aligned}$$

Differentiating gives two terms given by the derivative of the kernel and the derivative of the volume term (defined in Eq. (7)). The derivative of the kernel is

$$\partial_\varepsilon K_1(m_c(\mathbf{x} + \varepsilon \mathbf{h}), m_{c'}(\mathbf{x}'))|_{\varepsilon=0} = \frac{1}{d+1} \sum_{j=0}^d \nabla_1 K_1(m_c(\mathbf{x}), m_{c'}(\mathbf{x}'))^T h_{c_j}.$$

The derivative of the determinant in Eq. (7) gives:

$$\begin{aligned} & \partial_\varepsilon |\gamma_c(\mathbf{x} + \varepsilon \mathbf{h})| \\ &= \frac{1}{d!} \sum_{j=1}^d \det \left(x_{c_1} - x_{c_0}, \dots, x_{c_{j-1}} - x_{c_0}, h_{c_j} - h_{c_0}, x_{c_{j+1}} - x_{c_0}, x_{c_d} - x_{c_0} \right) \\ &= \frac{1}{d!} \sum_{j=1}^d (-1)^{j-1} \det \left(h_{c_j} - h_{c_0}, x_{c_1} - x_{c_0}, \dots, x_{c_{j-1}} - x_{c_0}, x_{c_{j+1}} - x_{c_0}, x_{c_d} - x_{c_0} \right) \\ &= \frac{1}{d!} \sum_{j=1}^d (h_{c_j} - h_{c_0})^T n_{c,j} \\ &= \frac{1}{d!} \sum_{j=0}^d h_{c_j}^T n_{c,j} \end{aligned}$$

where the last two equations use Eq. (17a) and Eq. (17c), respectively.

Collecting terms involving h_j gives the variation:

$$(31) \quad \begin{aligned} & \frac{1}{d+1} \sum_{c \in \mathcal{C}, c' \in \mathcal{C}'} \alpha_c \alpha_{c'} |\gamma_c(\mathbf{x})| |\gamma_{c'}(\mathbf{x}')| \langle \zeta_c, \zeta_{c'} \rangle_{W_2^*} \nabla_1 K_1(m_c(\mathbf{x}), m_{c'}(\mathbf{x}'))^T \left(\sum_{j=0}^d h_{c_j} \right) \\ & \quad + \frac{1}{d!} \sum_{c \in \mathcal{C}, c' \in \mathcal{C}'} \alpha_c \alpha_{c'} |\gamma_{c'}(\mathbf{x}')| \langle \zeta_c, \zeta_{c'} \rangle_{W_2^*} K_1(m_c(\mathbf{x}), m_{c'}(\mathbf{x}')) \left(\sum_{j=0}^d n_{c_j}^T h_{c_j} \right). \end{aligned}$$

Removing dependence on the perturbation direction gives the partial derivative

$$\begin{aligned} & \partial_{x_j} \langle \mu_{(S, \mathbf{x}, \boldsymbol{\alpha}, \boldsymbol{\zeta})}, \mu_{(S', \mathbf{x}', \boldsymbol{\alpha}', \boldsymbol{\zeta}')} \rangle_{W^*} = \\ & \quad \sum_{c \in \mathcal{C}: j \in c} \sum_{c' \in \mathcal{C}'} \alpha_c \alpha_{c'} |\gamma_{c'}(\mathbf{x}')| \langle \zeta_c, \zeta_{c'} \rangle_{W_2^*} \left(\frac{1}{d+1} |\gamma_c(\mathbf{x})| \nabla_1 K_1(m_c(\mathbf{x}), m_{c'}(\mathbf{x}')) \right. \\ & \quad \left. + \frac{1}{d!} K_1(m_c(\mathbf{x}), m_{c'}(\mathbf{x}')) n_c(x_j) \right) \end{aligned}$$

where $n_c(x_j)$ is the inward weighted normal to the face opposed to x_j in $\gamma(c)$. We finally get the expression of the gradient of the data attachment term as

$$\partial_{x_j} \|\mu_{(S^{(0)}, \mathbf{x}, \boldsymbol{\zeta}^{(0)})} - \mu_{\mathcal{T}^{(1)}}\|_{W^*}^2 = 2 \partial_{x_j} \langle \mu_{(S^{(0)}, \mathbf{x}, \boldsymbol{\zeta}^{(0)})}, \mu_{(S^{(0)}, \tilde{\mathbf{x}}, \boldsymbol{\zeta})} - \mu_{\mathcal{T}^{(1)}} \rangle_{W^*}.$$

evaluated with $\tilde{\mathbf{x}} = \mathbf{x}$.

□

CONFLICT OF INTEREST

MM owns a founder share of Anatomy Works with the arrangement being managed by Johns Hopkins University in accordance with its conflict of interest policies. The remaining authors declare that the research was conducted in the absence of

any commercial or financial relationships that could be construed as a potential conflict of interest.

ACKNOWLEDGEMENTS

Authors would like to acknowledge the Allen Institute for their support via the data contribution.

This work was supported by the National Institutes of Health (NIH) grants R01EB020062 (MM), R01NS102670 (MM), U19AG033655 (MM), P41-EB031771 (MM), and R01MH105660 (MM); the National Science Foundation (NSF) 16-569 NeuroNex contract 1707298 (MM); and the Computational Anatomy Science Gateway (MM) as part of the Extreme Science and Engineering Discovery Environment (XSEDE Towns et al., 2014), which is supported by the NSF grant ACI1548562, and the Kavli Neuroscience Discovery Institute supported by the Kavli Foundation (MM).

REFERENCES

- [1] Frederick J Almgren. *Plateau's problem: an invitation to varifold geometry*, volume 13. American Mathematical Soc., 1966.
- [2] Nachman Aronszajn. Theory of reproducing kernels. *Transactions of the American Mathematical Society*, 68(3):337–404, 1950.
- [3] J Ashburner. Computational anatomy with the spm software. *Magnetic Resonance Imaging*, 27:1163–1174, October 2009.
- [4] B. Avants and J. C. Gee. Geodesic estimation for large deformation anatomical shape averaging and interpolation. *Neuroimage*, 23 Suppl 1:S139–50, 2004. ISSN 1053-8119 (Print) 1053-8119 (Linking). doi: 10.1016/j.neuroimage.2004.07.010.
- [5] M.F. Beg, M.I. Miller, A. Trouvé, and L. Younes. Computing large deformation metric mappings via geodesic flows of diffeomorphisms. *International Journal of Computer Vision*, 61(2):139–157, 2005. ISSN 1573-1405. doi: 10.1023/B:VISI.0000043755.93987.aa.
- [6] Mirza Faisal Beg, Michael Miller, Alain Trouvé, and Laurent Younes. Computing large deformation metric mappings via geodesic flows of diffeomorphisms. *International Journal of Computer Vision*, 61:139–157, 02 2005. doi: 10.1023/B:VISI.0000043755.93987.aa.
- [7] Stephane Bugeon, Joshua Duffield, Mario Dipoppa, Anne Ritoux, Isabelle Pranker, Dimitris Nicolout-sopoulos, David Orme, Maxwell Shinn, Han Peng, Hamish Forrest, Aiste Viduolyte, Charu Bai Reddy, Yoh Isogai, Matteo Carandini, and Kenneth D. Harris. A transcriptomic axis predicts state modulation of cortical interneurons. *bioRxiv*, page 2021.10.24.465600, 2021. doi: 10.1101/2021.10.24.465600.
- [8] N. Charon and A. Trouvé. The varifold representation of nonoriented shapes for diffeomorphic registration. *SIAM Journal on Imaging Sciences*, 6(4):2547–2580, 2013. doi: 10.1137/130918885.
- [9] K. H. Chen, A. N. Boettiger, J. R. Moffitt, S. Wang, and X. Zhuang. Rna imaging. spatially resolved, highly multiplexed rna profiling in single cells. *Science*, 348(6233):aaa6090, 2015. ISSN 1095-9203 (Electronic) 0036-8075 (Linking). doi: 10.1126/science.aaa6090.

- [10] X. Chen, Y. C. Sun, H. Zhan, J. M. Kebschull, S. Fischer, K. Matho, Z. J. Huang, J. Gillis, and A. M. Zador. High-throughput mapping of long-range neuronal projection using in situ sequencing. *Cell*, 179(3):772–786 e19, 2019. ISSN 1097-4172 (Electronic) 0092-8674 (Linking). doi: 10.1016/j.cell.2019.09.023.
- [11] Elliott Ward Cheney and William Allan Light. *A course in approximation theory*, volume 101. American Mathematical Soc., 2009.
- [12] C. Condylis, A. Ghanbari, N. Manjrekar, K. Bistrong, S. Yao, Z. Yao, T. N. Nguyen, H. Zeng, B. Tasic, and J. L. Chen. Dense functional and molecular readout of a circuit hub in sensory cortex. *Science*, 375(6576): eabl5981, 2022. ISSN 1095-9203 (Electronic) 0036-8075 (Linking). doi: 10.1126/science.abl5981.
- [13] Hong Wei Dong. *The Allen reference atlas: A digital color brain atlas of the C57Bl/6J male mouse*. John Wiley and Sons Inc, 2008. ISBN 0470054085.
- [14] J. R. Ecker, D. H. Geschwind, A. R. Kriegstein, J. Ngai, P. Osten, D. Poliodakis, A. Regev, N. Sestan, I. R. Wickersham, and H. Zeng. The brain initiative cell census consortium: Lessons learned toward generating a comprehensive brain cell atlas. *Neuron*, 96(3):542–557, 2017. ISSN 1097-4199 (Electronic) 0896-6273 (Linking). doi: 10.1016/j.neuron.2017.10.007.
- [15] J. Glaunes, A. Trouvé, and L. Younes. Diffeomorphic matching of distributions: A new approach for unlabelled point-sets and sub-manifolds matching. *Lecture Notes in Computer Science*, 2004.
- [16] Joan Glaunes, Alain Trouvé, and Laurent Younes. Diffeomorphic matching of distributions: A new approach for unlabelled point-sets and sub-manifolds matching. In *Computer Vision and Pattern Recognition, 2004. CVPR 2004. Proceedings of the 2004 IEEE Computer Society Conference on*, volume 2, pages II–712. Ieee, 2004.
- [17] Ulf Grenander and Michael I Miller. Computational anatomy: An emerging discipline. *Quarterly of Applied Mathematics*, 56(4):617–694, 1998. ISSN 0033569X.
- [18] M. Helmstaedter. Cellular-resolution connectomics: challenges of dense neural circuit reconstruction. *Nat Methods*, 10(6):501–7, 2013. ISSN 1548-7105 (Electronic) 1548-7091 (Linking). doi: 10.1038/nmeth.2476.
- [19] Armin Iske. *Approximation theory and algorithms for data analysis*. Springer, 2018.
- [20] S. Joshi and M. I. Miller. Landmark matching via large deformation diffeomorphisms. *IEEE Trans. Image Processing*, 9(8):1357–1370, August 2000.
- [21] J. M. Kebschull, P. Garcia da Silva, A. P. Reid, I. D. Peikon, D. F. Albeanu, and A. M. Zador. High-throughput mapping of single-neuron projections by sequencing of barcoded rna. *Neuron*, 91(5):975–987, 2016. ISSN 1097-4199 (Electronic) 0896-6273 (Linking). doi: 10.1016/j.neuron.2016.07.036.
- [22] J. M. Kebschull, E. B. Richman, N. Ringach, D. Friedmann, E. Albarran, S. S. Kolluru, R. C. Jones, W. E. Allen, Y. Wang, S. W. Cho, H. Zhou, J. B. Ding, H. Y. Chang, K. Deisseroth, S. R. Quake, and L. Luo. Cerebellar nuclei evolved by repeatedly duplicating a conserved cell-type set. *Science*, 370(6523), 2020. ISSN 1095-9203 (Electronic) 0036-8075 (Linking). doi: 10.1126/science.abd5059.

- [23] Y. Kim, K. U. Venkataraju, K. Pradhan, C. Mende, J. Taranda, S. C. Turaga, I. Arganda-Carreras, L. Ng, M. J. Hawrylycz, K. S. Rockland, H. S. Seung, and P. Osten. Mapping social behavior-induced brain activation at cellular resolution in the mouse. *Cell Rep*, 10(2):292–305, 2015. ISSN 2211-1247 (Electronic). doi: 10.1016/j.celrep.2014.12.014.
- [24] Y. Kim, G. R. Yang, K. Pradhan, K. U. Venkataraju, M. Bota, L. C. Garcia Del Molino, G. Fitzgerald, K. Ram, M. He, J. M. Levine, P. Mitra, Z. J. Huang, X. J. Wang, and P. Osten. Brain-wide maps reveal stereotyped cell-type-based cortical architecture and subcortical sexual dimorphism. *Cell*, 171(2):456–469 e22, 2017. ISSN 1097-4172 (Electronic) 0092-8674 (Linking). doi: 10.1016/j.cell.2017.09.020.
- [25] Daniel D Lee and H Sebastian Seung. Algorithms for non-negative matrix factorization. In *Advances in neural information processing systems*, pages 556–562, 2001.
- [26] Michael Miller, Daniel Tward, and Alain Trouve. Molecular computational anatomy: Unifying the molecular to tissue continuum via measure representations of the brain. *Science Partner Journal*, 2022.
- [27] Michael I Miller, Alain Trouvé, and Laurent Younes. Geodesic Shooting for Computational Anatomy. *Journal of Mathematical Imaging and Vision*, 24(2): 209–228, 2006. ISSN 15737683. doi: 10.1007/s10851-005-3624-0.
- [28] Michael I Miller, Alain Trouvé, and Laurent Younes. Hamiltonian systems and optimal control in computational anatomy: 100 years since d’arcy thompson. *Annual Review of Biomed Engineering*, 17:447–509, November 4 2015.
- [29] Michael I Miller, Daniel J Tward, and Alain Trouvé. Coarse-to-fine hamiltonian dynamics of hierarchical flows in computational anatomy. In *Proceedings of the IEEE/CVF Conference on Computer Vision and Pattern Recognition Workshops*, pages 860–861, 2020.
- [30] Michael I Miller, Daniel Jacob Tward, and Alain Trouvé. Hierarchical computational anatomy: Unifying the molecular to tissue continuum via measure representations of the brain. *bioRxiv*, 2021.
- [31] J. R. Moffitt, D. Bambah-Mukku, S. W. Eichhorn, E. Vaughn, K. Shekhar, J. D. Perez, N. D. Rubinstein, J. Hao, A. Regev, C. Dulac, and X. Zhuang. Molecular, spatial, and functional single-cell profiling of the hypothalamic preoptic region. *Science*, 362(6416), 2018. ISSN 1095-9203 (Electronic) 0036-8075 (Linking). doi: 10.1126/science.aau5324.
- [32] Jeffrey R. Moffitt, Dhananjay Bambah-Mukku, Stephen W. Eichhorn, Eric Vaughn, Karthik Shekhar, Julio D. Perez, Nimrod D. Rubinstein, Junjie Hao, Aviv Regev, Catherine Dulac, and Xiaowei Zhuang. Molecular, spatial, and functional single-cell profiling of the hypothalamic preoptic region. *Science*, 362(6416), 2018. ISSN 0036-8075. doi: 10.1126/science.aau5324.
- [33] David Bryant Mumford and Jayant Shah. Optimal approximations by piecewise smooth functions and associated variational problems. *Communications on pure and applied mathematics*, 1989.
- [34] Arun Narasimhan, Kannan Umadevi Venkataraju, Judith Mizrachi, Dinu F. Albeanu, and Pavel Osten. Oblique light-sheet tomography: fast and high resolution volumetric imaging of mouse brains. *bioRxiv*, 2017. doi: 10.1101/132423.

- [35] S. W. Oh, J. A. Harris, L. Ng, B. Winslow, N. Cain, S. Mihalas, Q. Wang, C. Lau, L. Kuan, A. M. Henry, M. T. Mortrud, B. Ouellette, T. N. Nguyen, S. A. Sorensen, C. R. Slaughterbeck, W. Wakeman, Y. Li, D. Feng, A. Ho, E. Nicholas, K. E. Hirokawa, P. Bohn, K. M. Joines, H. Peng, M. J. Hawrylycz, J. W. Phillips, J. G. Hohmann, P. Wahnoutka, C. R. Gerfen, C. Koch, A. Bernard, C. Dang, A. R. Jones, and H. Zeng. A mesoscale connectome of the mouse brain. *Nature*, 508(7495):207–14, 2014. ISSN 1476-4687 (Electronic) 0028-0836 (Linking). doi: 10.1038/nature13186.
- [36] P. Osten and T. W. Margrie. Mapping brain circuitry with a light microscope. *Nat Methods*, 10(6):515–23, 2013. ISSN 1548-7105 (Electronic) 1548-7091 (Linking). doi: 10.1038/nmeth.2477.
- [37] X Pennec. From Riemannian Geometry to Computational Anatomy. *Elements*, 2011.
- [38] T. Ragan, L. R. Kadiri, K. U. Venkataraju, K. Bahlmann, J. Sutin, J. Taranda, I. Arganda-Carreras, Y. Kim, H. S. Seung, and P. Osten. Serial two-photon tomography for automated ex vivo mouse brain imaging. *Nat Methods*, 9(3):255–258, 2012. ISSN 1548-7105 (Electronic) 1548-7091 (Linking).
- [39] Robert Schaback and Holger Wendland. Kernel techniques: from machine learning to meshless methods. *Acta numerica*, 15:543–639, 2006.
- [40] Sheel Shah, Eric Lubeck, Wen Zhou, and Long Cai. In situ transcription profiling of single cells reveals spatial organization of cells in the mouse hippocampus. *Neuron*, 92(2):342–357, 2016. ISSN 0896-6273.
- [41] Kaitlin M Stouffer, Zhenzhen Wang, Eileen Xu, Karl Lee, Paige Lee, Michael I Miller, and Daniel J Tward. From picoscale pathology to decascale disease: Image registration with a scattering transform and varifolds for manipulating multiscale data. In *International Workshop on Multimodal Learning for Clinical Decision Support*, pages 1–11. Springer, 2021.
- [42] Y. C. Sun, X. Chen, S. Fischer, S. Lu, H. Zhan, J. Gillis, and A. M. Zador. Integrating barcoded neuroanatomy with spatial transcriptional profiling enables identification of gene correlates of projections. *Nat Neurosci*, 24(6):873–885, 2021. ISSN 1546-1726 (Electronic) 1097-6256 (Linking). doi: 10.1038/s41593-021-00842-4.
- [43] Alain Trouvé and François-Xavier Vialard. Shape Splines and Stochastic Shape Evolutions: A Second Order Point of View. *Quarterly of Applied Mathematics*, page 26, 2010.
- [44] M. Vaillant and J. Glaunes. Surface matching via currents. In G.E. Christensen and M. Sonka, editors, *IPMI*, volume 3565 of *Lecture Notes in Computer Science*, pages 381–392. Springer, 2005. ISBN 3-540-26545-7.
- [45] F-X Vialard, L Risser, D Rueckert, and CJ Cotter. 3d image registration via geodesic shooting using and efficient adjoint calculation. *Journal International Journal of Computer Vision*, 97(2):229–241, April 2012.
- [46] Quanxin Wang, Song-Lin Ding, Yang Li, Josh Royall, David Feng, Phil Lesnar, Nile Graddis, Maitham Naeemi, Benjamin Facer, and Anh Ho. The allen mouse brain common coordinate framework: A 3d reference atlas. *Cell*, 2020. ISSN 0092-8674.
- [47] X. Wang, W. E. Allen, M. A. Wright, E. L. Sylwestrak, N. Samusik, S. Vesuna, K. Evans, C. Liu, C. Ramakrishnan, J. Liu, G. P. Nolan, F. A. Bava, and

- K. Deisseroth. Three-dimensional intact-tissue sequencing of single-cell transcriptional states. *Science*, 361(6400), 2018. ISSN 1095-9203 (Electronic) 0036-8075 (Linking). doi: 10.1126/science.aat5691.
- [48] C. Xia, J. Fan, G. Emanuel, J. Hao, and X. Zhuang. Spatial transcriptome profiling by merfish reveals subcellular rna compartmentalization and cell cycle-dependent gene expression. *Proc Natl Acad Sci U S A*, 116(39):19490–19499, 2019. ISSN 1091-6490 (Electronic) 0027-8424 (Linking). doi: 10.1073/pnas.1912459116.
- [49] A.C. Xiaowei. Method of the year 2020: spatially resolved transcriptomics. *Nat Methods*, 18(1):1, 2021. ISSN 1548-7105 (Electronic) 1548-7091 (Linking). doi: 10.1038/s41592-020-01042-x.
- [50] S. Xu, H. Yang, V. Menon, A. L. Lemire, L. Wang, F. E. Henry, S. C. Turaga, and S. M. Sternson. Behavioral state coding by molecularly defined paraventricular hypothalamic cell type ensembles. *Science*, 370(6514), 2020. ISSN 1095-9203 (Electronic) 0036-8075 (Linking). doi: 10.1126/science.abb2494.
- [51] Laurent Younes. *Shapes and Diffeomorphisms*. Applied Mathematical Sciences. Springer-Verlag, Berlin Heidelberg, 2 edition, 2019. ISBN 978-3-662-58495-8. doi: 10.1007/978-3-662-58496-5.
- [52] Ron Zeira, Max Land, and Benjamin J. Raphael. Alignment and integration of spatial transcriptomics data. *bioRxiv*, page 2021.03.16.435604, 2021. doi: 10.1101/2021.03.16.435604.
- [53] Hongkui Zeng. unpublished data, 2022.
- [54] Ting Zheng, Zhongqing Yang, Anan Li, Xiaohua Lv, Zhenqiao Zhou, Xiaojun Wang, Xiaoli Qi, Shiwei Li, Qingming Luo, and Hui Gong. Visualization of brain circuits using two-photon fluorescence micro-optical sectioning tomography. *Optics express*, 21(8):9839–9850, 2013. ISSN 1094-4087.
- [55] B. Zingg, H. Hintiryan, L. Gou, M. Y. Song, M. Bay, M. S. Bienkowski, N. N. Foster, S. Yamashita, I. Bowman, A. W. Toga, and H. W. Dong. Neural networks of the mouse neocortex. *Cell*, 156(5):1096–1111, 2014. ISSN 1097-4172 (Electronic) 0092-8674 (Linking). doi: 10.1016/j.cell.2014.02.023.

MM: CENTER OF IMAGING SCIENCE AND DEPARTMENT OF BIOMEDICAL ENGINEERING, JOHNS HOPKINS UNIVERSITY

Email address: `mim@jhu.edu`

AT: CENTRE GIOVANNI BORELLI (UMR 9010), ECOLE NORMALE SUPÉRIEURE PARIS-SACLAY, UNIVERSITÉ PARIS-SACLAY

Email address: `alain.trouve@cmla.ens-cachan.fr`

LY: CENTER OF IMAGING SCIENCE AND DEPARTMENT OF APPLIED MATHEMATICS AND STATISTICS, JOHNS HOPKINS UNIVERSITY

Email address: `laurent.Younes@jhu.edu`